CrossMark

ORIGINAL PAPER

A model for CO₂ storage and seismic monitoring combining multiphase fluid flow and wave propagation simulators. The Sleipner-field case

Gabriela B. Savioli[1] · Juan E. Santos[1,2,3] · José M. Carcione[4] · Davide Gei[4]

Abstract The main objective of this paper is to use a flow simulator to represent the CO₂ storage and combine it with a wave propagation simulator in order to obtain synthetic seismograms qualitatively matching time-lapse real field data. The procedure is applied to the Utsira formation at Sleipner field. The field data at the site available to us is a collection of seismic sections (time-lapse seismics) used to monitor the CO₂ storage. An estimate of the CO₂ injection rate and the location of the injection point are known. Using these data, we build a geological model, including intramudstone layers with openings, whose coordinates are defined by performing a qualitative match of the field seismic data. The flow simulator parameters and the petrophysical properties are updated to obtain CO₂ saturation maps, including CO₂ plumes, so that the synthetic seismic images resemble the real data. The geological model is based on a porous-media constitutive equation. It considers a poroelastic description of the Utsira formation (a shaly sandstone), based on porosity and clay content, and takes into account the variation of the properties with pore pressure and fluid saturation. Moreover, the model considers the geometrical features of the formations, including the presence of shale seals and fractures. We also assume fractal variations of the petrophysical properties. The numerical simulation of the CO₂-brine flow is based on the Black-Oil formulation, which uses the pressure-volume-temperature (PVT) behavior as a simplified thermodynamic model. The corresponding equations are solved using a finite difference IMPES formulation. Using the resulting saturation and pore-pressure maps, we determine an equivalent viscoelastic medium at the macroscale, formulated in the space-frequency domain. Wave attenuation and velocity dispersion, caused by heterogeneities formed of gas patches, are described with White's mesoscopic model. The viscoelastic wave equation is solved in the space-frequency domain for a collection of frequencies of interest using a finite-element iterative domain decomposition algorithm. The space-time solution is recovered by a discrete inverse Fourier transform, allowing us to obtain our synthetic seismograms. In the numerical examples, we determine a set of flow and petrophysical parameters allowing us to obtain synthetic seismograms resembling actual field data. In particular, this approach yields CO₂ accumulations below the mudstone layers and synthetic seismograms which successfully reproduce the typical pushdown effect.

Keywords Multiphase fluid flow · CO₂ injection and storage · Wave propagation · Synthetic seismograms

✉ Gabriela B. Savioli
   gbsavioli@yahoo.com.ar

1   Universidad de Buenos Aires, Facultad de Ingeniería,
    Instituto del Gas y del Petróleo, Av. Las Heras 2214 Piso 3
    ŁC1127AAR, Buenos Aires, Argentina

2   Department of Mathematics, Purdue University,
    West Lafayette, IN 47907, USA

3   Universidad Nacional de La Plata, Buenos Aires, Argentina

4   Istituto Nazionale di Oceanografia e di Geofisica
    Sperimentale, Trieste, Italy

1 Introduction

Capture and storage of carbon dioxide in deep saline aquifers and aging oil reservoirs are a valid alternative

approach for reducing the amount of greenhouse gases in the atmosphere [1]. Saline aquifers are suitable as storage sites due to their large volume and their common occurrence in nature. The first industrial scale CO_2 injection project is the Sleipner gas field in the North Sea, where CO_2 separated from natural gas, is being injected in the Utsira formation, a highly permeable porous sandstone 800 m below the sea bottom. Within the formation, there are several mudstone layers which act as barriers to the vertical flow of the CO_2. Injection started in 1996 at a rate of about one million tonnes per year [1, 2].

Nevertheless, very little is known about the behavior of stored CO_2 over very long periods. Numerical modeling of CO_2 injection and seismic monitoring are important tools to understand the long-term behavior after injection and to test the effectiveness of CO_2 sequestration. Recent papers [3–5] successfully apply seismic modeling for monitoring the spatio-temporal distribution of CO_2 using assumed saturation maps. Instead, we introduce a methodology to model the gas flow and monitor the storage. For this purpose, we perform numerical simulations of CO_2-brine flow and seismic wave propagation. We build a petrophysical model of the Utsira formation based on fractal porosity and clay content, taking into account the variation of properties with pore pressure and saturation [6]. This model also includes embedded mudstone layers of very low permeability that accumulate CO_2 but also allow its migration. The simultaneous flow of brine and CO_2 is modeled with the Black-Oil formulation for two-phase flow in porous media [7], which uses the PVT data as a simplified thermodynamic model [8]. The pressure map before the injection is assumed to be hydrostatic for which a reference porosity map is defined. The permeability is assumed to be anisotropic and is obtained from first principles as a function of porosity and grain sizes [6].

The wave propagation is based on an isotropic viscoelastic model that considers dispersion and attenuation effects. It is well known that mesoscopic losses are the main attenuation mechanism in fluid saturated porous media. They are caused by heterogeneities in the fluid and solid phase properties greater than the pore size but much smaller than the predominant wavelengths [9, 10]. Since the size of the mesoscopic heterogeneities (e.g., gas patches) are of the order of mm and cm, it is not possible to use finite elements and finite difference methods with an explicit poroelastic description, because it requires an impractical number of grid points. Hence, we use an implicit description, representing the porous medium with a viscoelastic medium [11]. The complex P-wave and S-wave moduli are determined as follows: in the brine saturated mudstone layers we use a Zener model to represent the viscoelastic behavior of the material [12]; outside the mudstone layers, we assume a patchy CO_2-brine distribution and apply the simplest model of patchy saturation, which is the White's model for alternating CO_2-brine layers at the mesoscopic level [13]. The results of the flow simulator, applied to the petrophysical (poro-viscoelastic) model, allows us to calculate the phase velocities and attenuation coefficients of the P and S waves in order to compute the synthetic seismograms. Also, Dai el al. [14] performed numerical simulations of wave propagation in 2-D heterogeneous poroelastic media using finite difference techniques, but their model does not take into account mesoscopic-scale attenuation and dispersion effects at field scales.

The methodology is used to model CO_2 injection and flow and compute time-lapse seismograms corresponding to the Utsira aquifer at the Sleipner field. It is possible to identify the spatio-temporal distribution of CO_2 after its injection over long periods of time. Attenuation and dispersion effects are clearly observed in the recorded traces. The synthetic seismograms show the progressive increase in CO_2 accumulations below the mudstone layers and the pushdown effect observed in field data [15]. Better results are obtained by updating the petrophysical properties (mainly porosity, permeability and dry-rock moduli). Since the effectiveness of the time-lapse seismic method depends on the survey plan and the properties of the storage site [16], these simulations may be used to optimize the type of sources and the number and location of receivers to perform the seismic surveys. Time-lapse 3D surveys in different directions, computing a series of common shots and then performing the standard processing sequence may help to determine the CO_2 distribution within the Utsira formation.

2 The black-oil formulation of two-phase flow in porous media

The simultaneous flow of brine and CO_2 in porous media is described by the well-known Black-Oil formulation applied to two-phase, two component fluid flow [7]. We identify the CO_2 saturated aqueous phase (CO_2 and brine components, subindex b) with the oil phase and the CO_2 phase (subindex g) with the gas phase. In this way, the CO_2 component may dissolve in the aqueous phase but the brine component is not allowed to vaporize into the CO_2 phase. The differential equations are obtained by combining the mass conservation equations with Darcy's empirical Law.

The mass conservation equations are:

For the CO_2 component,

$$-\nabla \cdot (\rho_g \, v_g + C_{g,b} \, \rho_b \, v_b) + q_g = \frac{\partial \left[\phi \left(\rho_g S_g + C_{g,b} \, \rho_b \, S_b \right) \right]}{\partial t} ; \qquad (1)$$

for the brine component,

$$-\nabla \cdot (C_{b,b}\, \rho_b\, v_b) + q_b = \frac{\partial \left[\phi (C_{b,b}\, \rho_b\, S_b) \right]}{\partial t}, \quad (2)$$

where ρ is density at reservoir conditions, v is Darcy velocity, S is saturation, q mass rate of injection per unit volume and ϕ is porosity. $C_{g,b}$, $C_{b,b}$ are the mass fractions of CO_2 and brine in the brine phase, respectively. In the Black-Oil formulation, these fractions are computed using a simplified thermodynamic model as

$$C_{g,b} = \frac{R_s\, \rho_g^{SC}}{B_b\, \rho_b}, \quad C_{b,b} = \frac{\rho_b^{SC}}{B_b \rho_b}, \quad \rho_g = \frac{\rho_g^{SC}}{B_g} \quad (3)$$

where R_s (CO_2 solubility in brine), B_g (CO_2 formation volume factor) and B_b (brine formation volume factor) are the PVT data. Also ρ_g^{SC} and ρ_b^{SC} are the CO_2 and brine densities at standard conditions. To estimate the Black-Oil PVT data, we apply an algorithm developed by Hassanzadeh et al. [8], which is summarized in Section 4.2.

The Darcy's Law for two phase flow [7, 17] gives the momentum balance for the fluids,

$$v_g = -\underline{\kappa} \frac{\kappa_{rg}}{\eta_g} (\nabla p_g - \rho_g g \nabla D), \quad (4)$$

$$v_b = -\underline{\kappa} \frac{\kappa_{rb}}{\eta_b} (\nabla p_b - \rho_b g \nabla D), \quad (5)$$

where D indicates depth, generally identified with the coordinate z, and g is the gravity constant. Also, p_g, p_b are the fluid pressures and $\underline{\kappa}$ is the absolute permeability tensor, assumed to be diagonal $\underline{\kappa} = \text{diag}(\kappa_x, \kappa_y, \kappa_z)$. For $\beta = g, b$, the functions $k_{r\beta}$ and η_β are the relative permeability and viscosity of the β-phase, respectively. The relative permeability $k_{r\beta}$ is function of fluid saturation. Although Darcy's Law has been obtained empirically, it can be deduced from the Navier Stokes' equation for newtonian fluids [18].

Inserting Eqs. 3–5 into Eqs. 1–2 and dividing by ρ_g^{SC} and ρ_b^{SC}, the following nonlinear system of partial differential equations is obtained,

$$\nabla \cdot (\underline{\kappa}(\frac{\kappa_{rg}}{B_g \eta_g}(\nabla p_g - \rho_g g \nabla D) + \frac{R_s \kappa_{rb}}{B_b \eta_b}(\nabla p_b - \rho_b g \nabla D)))$$
$$+ \frac{q_g}{\rho_g^{SC}} = \frac{\partial \left[\phi \left(\frac{S_g}{B_g} + \frac{R_s S_b}{B_b} \right) \right]}{\partial t}, (6)$$

$$\nabla \cdot (\underline{\kappa} \frac{\kappa_{rb}}{B_b \eta_b}(\nabla p_b - \rho_b g \nabla D)) + \frac{q_b}{\rho_b^{SC}} = \frac{\partial \left[\phi \frac{S_b}{B_b} \right]}{\partial t}. \quad (7)$$

Two algebraic equations relating the saturations and pressures complete the system:

$$S_b + S_g = 1, \qquad p_g - p_b = P_C(S_b), \quad (8)$$

where P_C is the capillary pressure.

The unknowns for the Black-Oil model are the fluid pressures p_g, p_b and the saturations S_g, S_b for the CO_2 and brine phases, respectively. This flow model does not take into account chemical reactions.

The numerical solution is obtained with public-domain software BOAST [19] which solves the differential equations using the IMPES algorithm (Implicit Pressure Explicit Saturation), based on a finite difference technique [7]. Finite differences is the standard commercial reservoir simulator, and the improved versions use both structured and unstructured grids with local refinements to accurately represent reservoir geometry. The basic idea of IMPES is to obtain a single pressure equation by a combination of the flow equations; therefore, Eq. 6 multiplied by B_g and Eq. 7 multiplied by $(B_b - R_s B_g)$ are added. After some algebraic manipulations (the details may be seen in Appendix A) and replacing p_g by $p_b + P_C(S_b)$ in the left side of the combined equation, the following pressure equation in p_b is obtained,

$$B_g \Big[\nabla \cdot (\underline{\kappa}(\frac{\kappa_{rg}}{B_g \eta_g}(\nabla p_b - \rho_g g \nabla D)$$
$$+ \frac{R_s \kappa_{rb}}{B_b \eta_b}(\nabla p_b - \rho_b g \nabla D) + \frac{\kappa_{rg}}{B_g \eta_g}\nabla P_C)) \Big]$$
$$+ (B_b - R_s B_g)\Big[\nabla \cdot (\underline{\kappa} \frac{\kappa_{rb}}{B_b \eta_b}(\nabla p_b - \rho_b g \nabla D)) \Big]$$
$$+ B_g \frac{q_g}{\rho_g^{SC}} + (B_b - R_s B_g)\frac{q_b}{\rho_b^{SC}} = \phi c_t \frac{\partial p_b}{\partial t}, \quad (9)$$

where c_t is the total compressibility (see the definitions of compressibilities in Appendix A).

In the BOAST simulator, the nonlinear differential Eqs. 9 and 7 are discretized applying a backward finite difference scheme in a block centered grid. The discretized equations are linearized evaluating the pressure and saturation dependent coefficients (PVT parameters, viscosities, relative permeabilities and capillary pressure) using the pressure and saturation values at the previous time step. First, the pressure Eq. 9 is solved implicitly. The block successive over relaxation method (BSOR) is applied to compute the solution of the resulting linear system. Once the pressures for the new time are obtained, we compute the saturations explicitly from the discretization of Eq. 7. Consequently, the time step has to be selected according to the stability restrictions [20].

3 A viscoelastic model for wave propagation

One of the main phenomena occurring in rocks, in particular partially saturated with gas, is the mesoscopic-loss effect [12, 13]. It is caused by heterogeneities in the fluid and solid phase properties much larger than the pore size but much smaller than the predominant wavelengths. The mesoscopic-loss effect causes wave attenuation and velocity dispersion. The mesoscopic-loss peak frequency is proportional to the rock permeability and inversely proportional to the fluid viscosity (see [12]; eq. 7.499). It is the transition frequency separating the relaxed and unrelaxed states. At this reference frequency, the Biot slow-wave attenuation length equals the mean layer thickness or characteristic length of the inhomogeneities. The relaxation peak moves towards the low frequencies with increasing viscosity and decreasing permeability, i.e., the opposite behaviour of the Biot's relaxation mechanism.

Because the mesoscopic-scale is typically on the order of centimeters, in order to perform numerical simulations in these types of media using Biot's equations of motion at the macroscale, it is necessary to use extremely fine meshes to properly represent these heterogeneities and their attenuation effects on the fast (P and S) waves, which makes this procedure computationally very expensive or even not feasible. As an alternative to include mesoscopic-scale attenuation and dispersion effects, we use the simplest model for mesoscopic loss given in [13], which yields a complex plane wave modulus for the formation. We also determine a complex and frequency dependent shear modulus using another

relaxation mechanism related to the P-wave mechanism as in [5].

Let ρ_s and ρ_f be the grain and fluid densities, respectively. The equation of motion in a 2D isotropic viscoelastic domain Ω with boundary $\partial\Omega$ can be stated in the space-frequency (x, ω) domain as

$$-\omega^2 \rho u - \nabla \cdot \sigma(u) = f(x, \omega), \quad \Omega \tag{10}$$

$$-\sigma(u)\nu = i\omega \mathcal{D}u, \quad \Gamma = \partial\Omega, \tag{11}$$

where $u = (u_x, u_z)$ is the displacement vector and

$$\rho = (1 - \phi)\rho_s + \phi\rho_f \tag{12}$$

is the bulk density.

Equation 11 is a first-order absorbing boundary condition [21], where

$$\mathcal{D} = \rho \begin{bmatrix} \nu_1 & \nu_2 \\ -\nu_2 & \nu_1 \end{bmatrix} \begin{bmatrix} v_P(\omega) & 0 \\ 0 & v_S(\omega) \end{bmatrix} \begin{bmatrix} \nu_1 & -\nu_2 \\ \nu_2 & \nu_1 \end{bmatrix},$$

with $\nu = (\nu_1, \nu_2)$ the unit outward normal on Γ and $v_P(\omega)$, $v_S(\omega)$ the phase velocities of the compressional and shear waves at the frequency ω defined below in Eq. 14.

The stress tensor $\sigma(u)$ is defined in the space-frequency domain by

$$\sigma_{jk}(u) = \lambda_G(\omega)\nabla \cdot u\delta_{jk} + 2\mu(\omega)\varepsilon_{jk}(u), \quad \Omega, \tag{13}$$

where $\varepsilon_{jk}(u)$ denotes the strain tensor and δ_{jk} is the Kroenecker delta. The Lamé coefficients $\lambda_G(\omega)$ and $\mu(\omega)$ are

Fig. 1 Initial porosity distribution before CO$_2$ injection
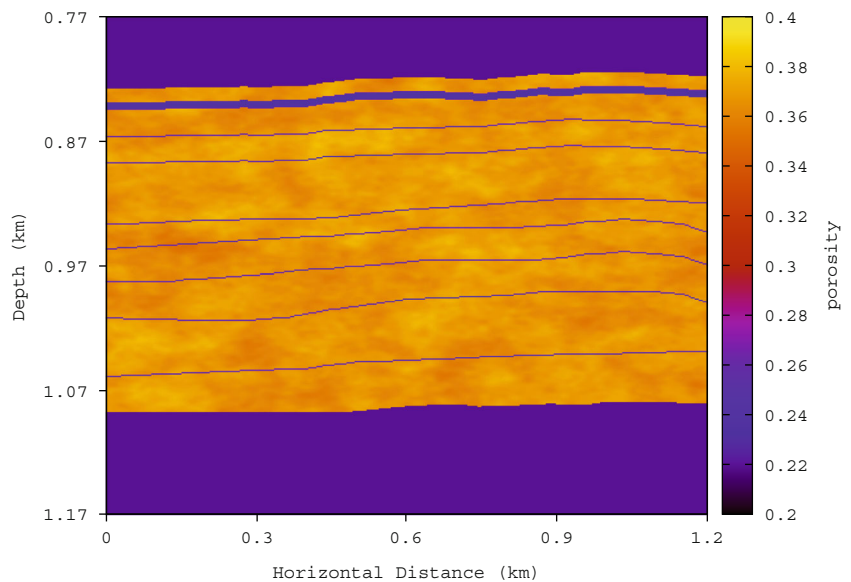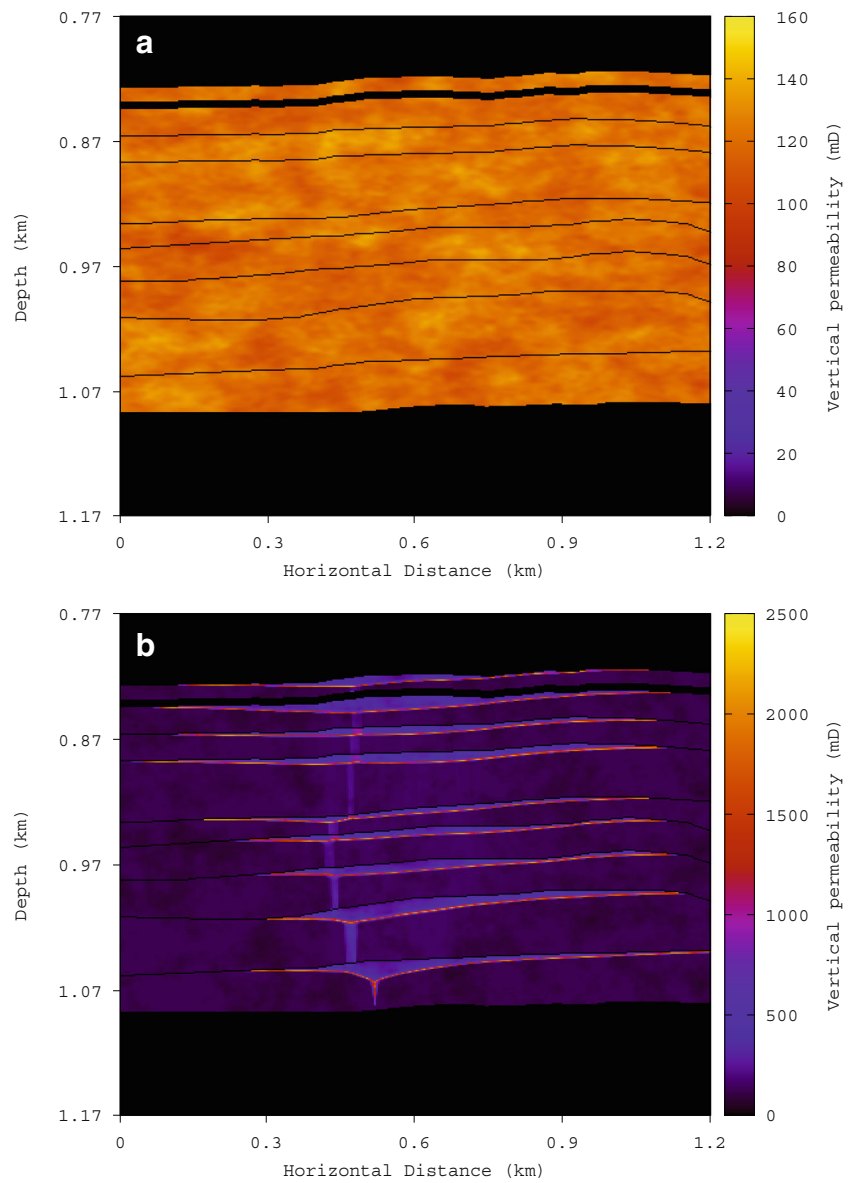
Fig. 2 Vertical permeability distribution: **a** before CO_2 injection and **b** after 7 years of CO_2 injection

complex and frequency dependent and are determined as follows. In the brine saturated mudstone layers these coefficients are obtained using a Zener model [12]. Outside the mudstone layers we consider P-wave attenuation due to wave induced fluid flow at mesoscopic scale, assuming a patchy CO_2-brine distribution and using the simplest model of patchy saturation, which is the White's theory of alternating CO_2-brine layers at the mesoscopic level [13]. We assume an alternating stack of two layers of thickness h_1 and h_2, with period $h = h_1 + h_2 = 80$ cm. The values of h_1 and h_2 are determined in terms of CO_2 saturation at each computational cell. These values are typically mesoscopic in terms of spatial scale, i.e., greater than the pore size and

much smaller than the wavelength. We use this approach since this is the most general theory, where any property can vary mesoscopically. This model can be applied in 2D and 3D as a good approximation to describe attenuation, and can be implemented with Zener elements as in [5]. This approach yields a complex and frequency dependent P-wave modulus $E(\omega) = \lambda_G(\omega) + 2\mu(\omega)$ for the formation. S-wave attenuation is also taken into account by making the shear modulus $\mu(\omega)$ complex and frequency dependent as explained in [5].

Both Zener and White models require the knowledge of the bulk and shear moduli K_s, μ_s and density ρ_s of the solid grains, the bulk and shear moduli K_m and μ_m as

Fig. 3 CO_2 saturation distribution: **a** after 1 year of CO_2 injection, **b** after 3 years of CO_2 injection, and **c** after 7 years of CO_2 injection
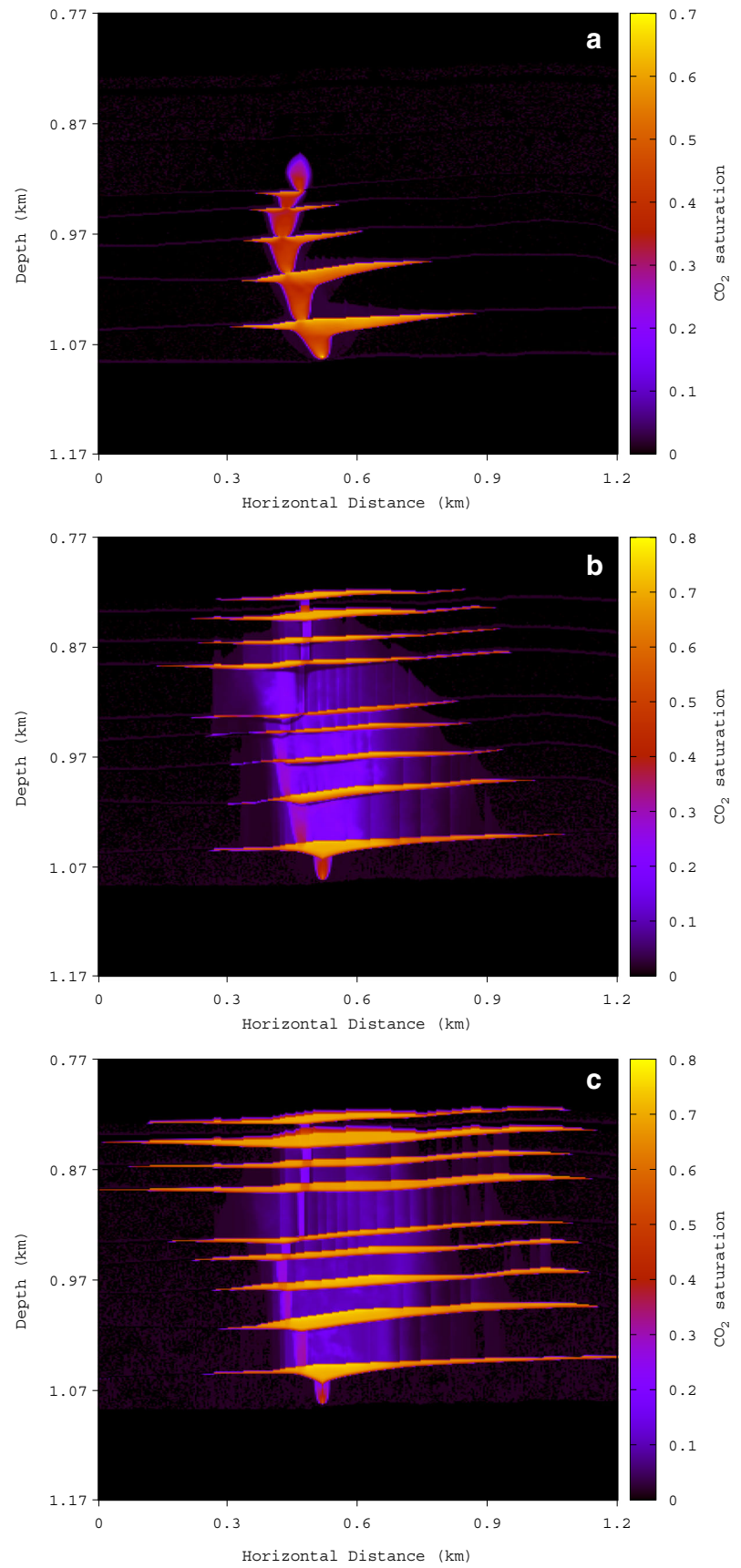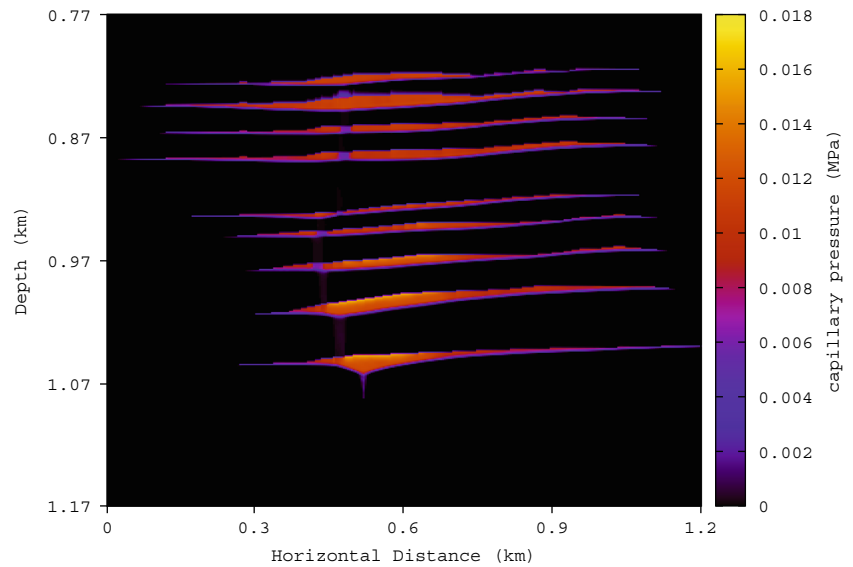
Fig. 4 Capillary pressure distribution after seven years of CO_2 injection

well as the porosity ϕ and permeabilities κ_x, κ_z of the solid matrix. They also need the fluid bulk modulus and viscosity. The determination of these parameters is explained in Section 4.1.

The phase velocities $v(\omega)$ and quality factors $Q(\omega)$ are defined by the relations

$$v_t(\omega) = \left[\text{Re} \left(\frac{1}{vc_t(\omega)} \right) \right]^{-1},$$

$$Q_t(\omega) = \frac{\text{Re}(vc_t(\omega)^2)}{\text{Im}(vc_t(\omega)^2)}, \quad t = P, S, \qquad (14)$$

where $vc_t(\omega)$ are the complex and frequency dependent compressional velocities defined as

$$vc_P(\omega) = \sqrt{\frac{E(\omega)}{\rho}}, \quad vc_S(\omega) = \sqrt{\frac{\mu(\omega)}{\rho}}. \qquad (15)$$

The quality factor measures the attenuation of the P and S waves; the lower the Q_p value, the higher the attenuation of P-waves and similarly for S-waves.

The solution of the differential system (10)–(11) is computed by using an iterative finite-element domain decomposition procedure, formulated in the space-frequency domain. In this approach, the solution is computed at a selected number of frequencies in the range of interest, defined in terms of the source spectrum, and the space-time solution is determined by using a discrete inverse Fourier transform. The convergence of the procedure is demonstrated in [21], where numerical examples are also given. In our problem, the absorbing boundary condition (11) is used in all boundaries of the computational domain.

A detailed description of the iterative domain decomposition algorithm can be found in Appendix B.

4 Petrophysical, fluid-flow, and seismic data

In this section, we describe the procedure used to determine the petrophysical and fluid-flow parameters needed in the Black-Oil and seismic simulations.

4.1 A petrophysical model for the Utsira formation

The shaly sandstone model used here is that of Carcione et al. [22], where the topology of the sandy and shaly mixture has been defined to obtain the petrophysical properties of the Utsira formation.

The pressure dependence of properties is based on the following relationship between porosity and pore pressure $p(t) = S_b p_b(t) + S_g p_g(t)$,

$$\frac{(1 - \phi_c)}{K_s} (p(t) - p_H) = \phi_0 - \phi(t) + \phi_c \ln \frac{\phi(t)}{\phi_0}, \qquad (16)$$

where ϕ_c is a critical porosity, $\phi_0 = \phi_0(x, z)$ is the initial porosity at hydrostatic pore pressure p_H and K_s is the bulk modulus of the solid grains [6]. Porosity ϕ_0 is assumed to have a fractal spatial distribution around the average porosity $\langle \phi_0 \rangle$, obtained from the neutron log by using standard methods. The rock is formed with quartz (bulk modulus of 40 GPa) and clay (bulk modulus of 15 GPa). K_s is computed as the arithmetic average of the Hashin Shtrikman upper and lower bounds [23].

Fig. 5 P-wave velocity: **a** before CO_2 injection and **b** after 7 years of CO_2 injection
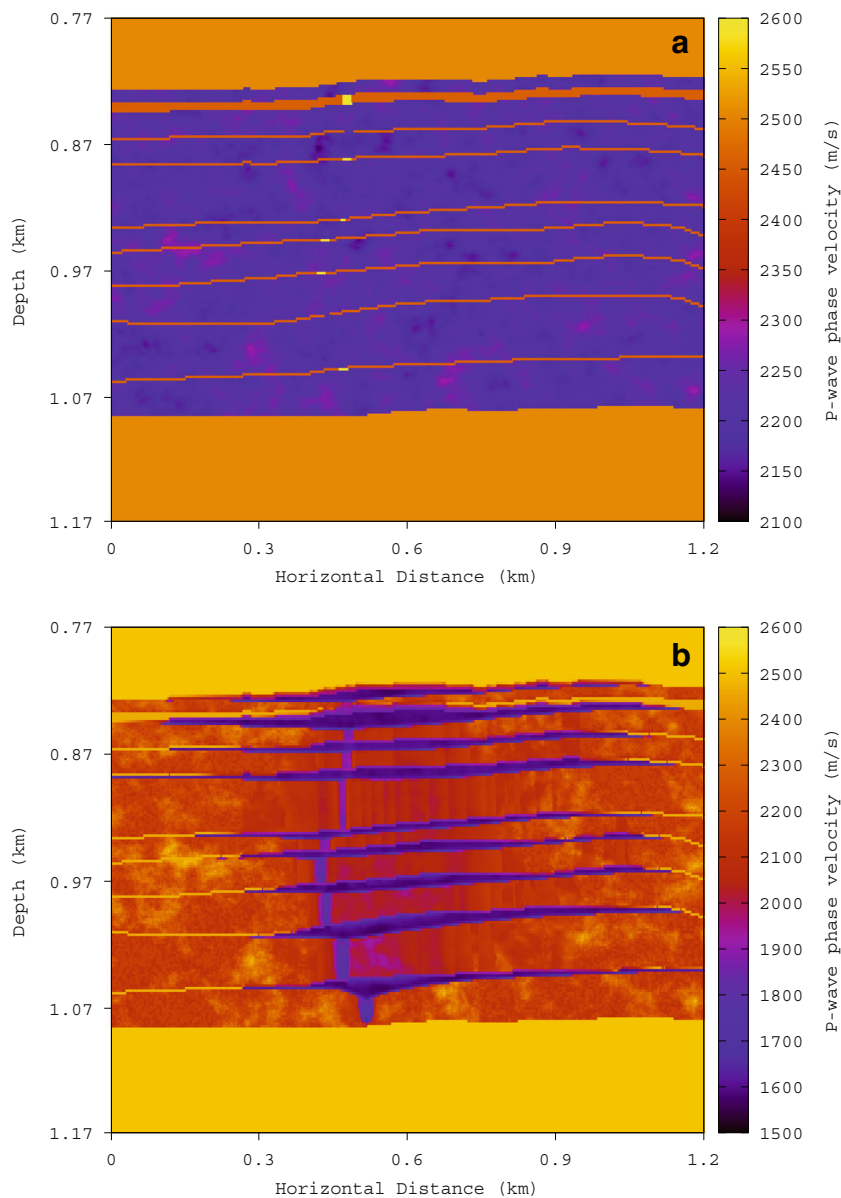
The relationship among horizontal permeability, porosity and clay content C is [6],

$$\frac{1}{\kappa_x(t)} = \frac{45(1-\phi(t))^2}{\phi(t)^3}\left(\frac{(1-C)^2}{R_q^2} + \frac{C^2}{R_c^2}\right), \qquad (17)$$

where R_q and R_c are the average radii of the sand and clay grains.

Also, as permeability is anisotropic, we assume the following relationship between horizontal and vertical permeability κ_z [6]

$$\frac{\kappa_x(t)}{\kappa_z(t)} = \frac{1-(1-0.3a)\sin\pi S_b}{a(1-0.5\sin\pi S_b)}, \qquad (18)$$

where a is the permeability-anisotropy parameter.

The bulk and shear moduli of the dry matrix, K_m, μ_m are computed using the Krief relation [24] as follows:

$$K_m(t) = K_s(1-\phi(t))^{A/(1-\phi(t))}, \qquad (19)$$

$$\mu_m(t) = \mu_s(1-\phi(t))^{A/(1-\phi(t))}. \qquad (20)$$

Using the moduli K_s, μ_s, K_m, μ_m, the porosity ϕ and permeabilities κ_x, κ_z, as well as the fluids bulk moduli and viscosities (computed using the Peng-Robinson model [25]), we determine the complex and frequency dependent Lamé coefficients $\lambda(\omega), \mu(\omega)$ as explained in Section 3.

Fig. 6 S-wave velocity: **a** before CO$_2$ injection and **b** after 7 years of CO$_2$ injection
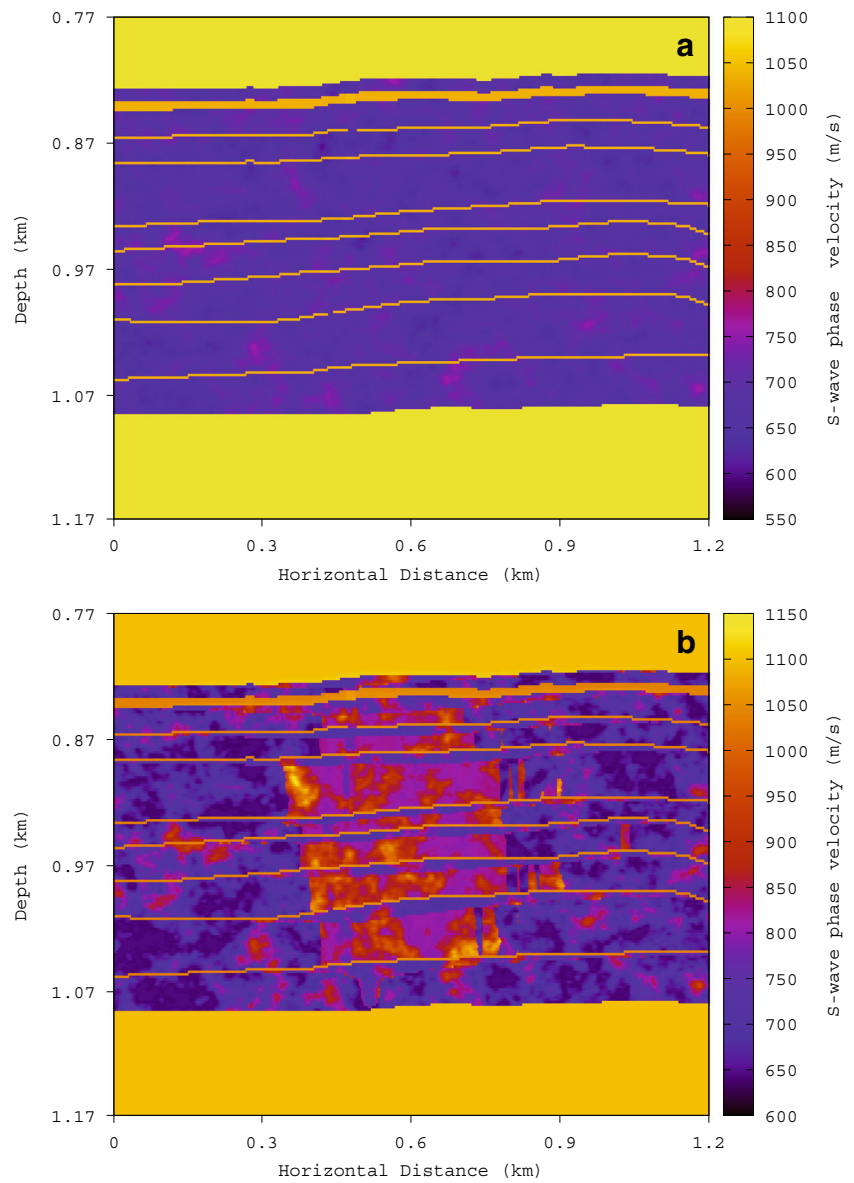
Relative permeabilities and capillary pressure as functions of CO$_2$ saturation are represented by the following potential models [20]:

$$\kappa_{rg}(S_g) = \kappa_{rg}^* \left(\frac{S_g - S_{gc}}{1 - S_{gc} - S_{bc}} \right)^{n_g}, \tag{21}$$

$$\kappa_{ro}(S_g) = \kappa_{ro}^* \left(\frac{1 - S_g - S_{bc}}{1 - S_{gc} - S_{bc}} \right)^{n_o}, \tag{22}$$

$$P_C(S_g) = P_C^* \left(\frac{S_g - S_{gc}}{1 - S_{gc} - S_{bc}} \right)^{n_c}, \tag{23}$$

where κ_{rg}^*, κ_{ro}^*, P_C^* are the maximum values of the curves and the exponents n_g, n_o, n_c determine the curvature. S_{gc},

S_{bc} are the saturations at which CO$_2$ and brine phases become mobile, respectively. The influence of capillary pressure on CO$_2$ injection, storage and monitoring is analysed in detail in [26].

4.2 The black oil fluid model

The PVT data, R_s and B_b, can be expressed in terms of the equilibrium properties obtained from an equation of state as presented in [8] and [27], i.e.,

$$R_s = \frac{\widetilde{\rho}_b^{SC} \chi_g}{\widetilde{\rho}_g^{SC}(1 - \chi_g)}, \quad B_b = \frac{\rho_b^{SC}}{\rho_b(1 - \omega_g)}, \tag{24}$$

where $\widetilde{\rho}_b^{SC}$ and $\widetilde{\rho}_g^{SC}$ are the brine and CO$_2$ molar densities at standard conditions, respectively, χ_g and ω_g are the

Fig. 7 P-wave quality factor Q_p at 50 Hz after 7 years of CO_2 injection
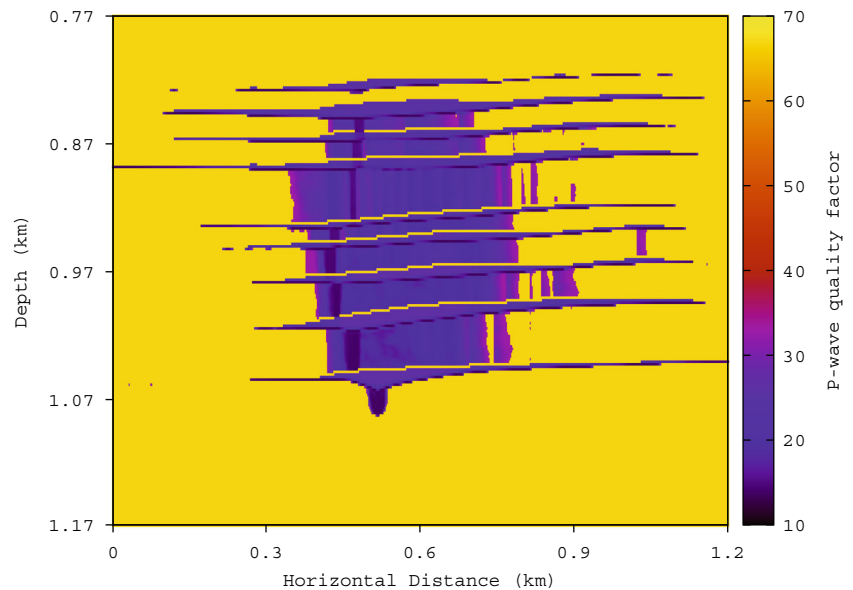
CO_2 mole and mass fractions in the brine phase. The molar density is related to the mass density through the molecular weight. While the CO_2 molecular weight (M_g) and mass density at standard conditions (ρ_g^{SC}) are known, these properties for the brine phase must be estimated. The brine molecular weight (M_b) is simply computed from the mole fractions χ_{salt} of NaCl and χ_{H_2O} of H_2O. The brine mass density at standard conditions, ρ_b^{SC}, is estimated following the Rowe and Chou correlation as given in formulas (B6)-(B14) of [8]. Once ρ_b^{SC} is computed, ρ_b at reservoir conditions is obtained using the approach of García, as stated in [8]. This approach and the estimation of the CO_2 mole and mass fractions in the brine phase, χ_g and ω_g, are briefly explained in Appendix C.

Finally, the viscosity, density, and bulk modulus of CO_2 are obtained from the Peng-Robinson equations as a function of temperature and pore pressure.

5 Numerical experiments

To test the proposed methodology, we consider a model of the Utsira formation having 1.2 km in the x-direction, 10 km in the y-direction and 0.4 km in the z-direction (top at 0.77 km and bottom at 1.17 km b.s.l.). The pressure-temperature conditions are $T = 31.7z + 3.4$, where T is the temperature (in °C) and z is the depth (in km b.s.l.); $p_H = \rho_b g z$ is the hydrostatic pressure, with $\rho_b = 1040$ kg/m³ the density of brine and g the gravity constant. Within the formation, there are several mudstone layers which act as barriers to the vertical motion of the CO_2.

The initial porosity $\phi_0 = \phi_0(x, z)$ at hydrostatic pore pressure for the Utsira sandstone (see Eq. 16) is assumed

to have a fractal spatial distribution, obtained as follows. First, we generate a fractal porosity distribution, based on the so-called von Karman self-similar correlation functions. These models are widely used in the statistical characterization of heterogeneities for different applications. The fractal porosity is obtained with the following relation

$$\phi_0(x, z) = \langle \phi_0 \rangle + f(x, z). \tag{25}$$

In Eq. 25 $\langle \phi_0 \rangle$ denotes the spatial average of $\phi_0(x, z)$ and $f(x, z)$ is a fractal field representing the spatial fluctuation of $\phi_0(x, z)$, for which the spectral density is given by [28]

$$S_d(r_x, r_z) = N_0(1 + R^2\alpha^2)^{-(H+E/2)}. \tag{26}$$

Here $R = \sqrt{r_x^2 + r_z^2}$ is the radial wavenumber, α the correlation length, H is a self-similarity coefficient ($0 < H < 1$), N_0 is a normalization constant and E is the euclidean dimension. The von Karman correlation (26) describes a self-affine, fractal processes of fractal dimension $D = E + 1 - H$ at a scale smaller than α. For this application we take $E = 2$, $D = 2.2$ and $\langle \phi_0 \rangle = 36.7$ %. The correlation length value was taken to be 2 % of the domain size. We generated a porosity field, by choosing the variance parameter in the fractal generator. Horizontal and vertical permeabilities were determined by using Eqs. 17 and 18, considering an anisotropy parameter $a = 0.1$ and a fixed clay content $C = 6$ %. The minimum, average and maximum porosities obtained are 32.5, 36.7, and 38.3 %, respectively. The associated vertical permeabilities are 0.1, 0.12, and 0.145 D. The mudstone layers are not completely sealed, having constant porosity and vertical permeability values of 24 % and 0.033 D. Besides they have openings, that will give a path for the

Fig. 8 Synthetic seismograms: **a** before CO_2 injection, **b** after one year of CO_2 injection, **c** after three years of CO_2 injection and **d** after seven years of CO_2 injection
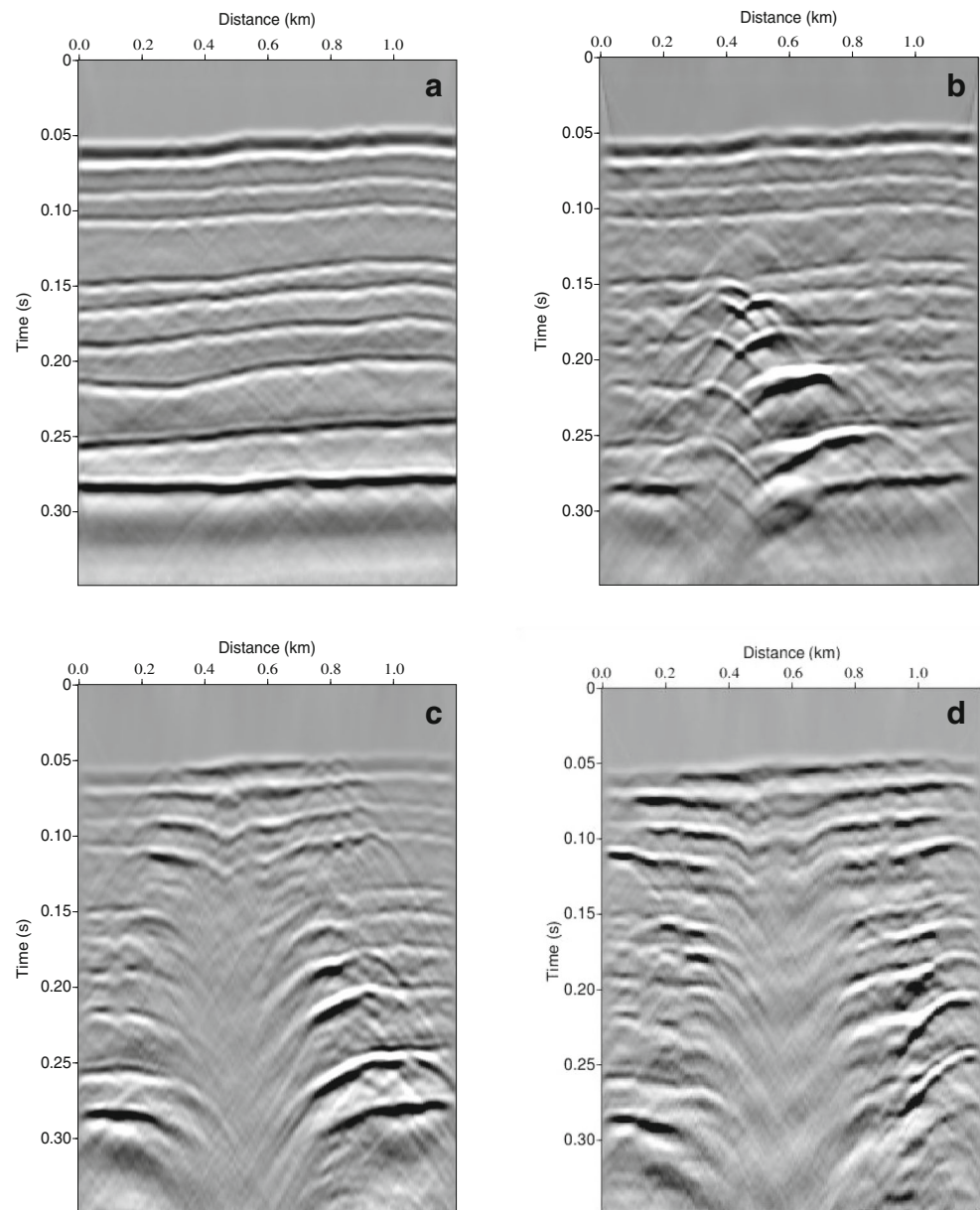

upward migration of CO_2. The top and bottom of the Utsira formation have constant porosity and vertical permeability values of 22 % and 0.02 D. The initial porosity and vertical permeability fields can be observed in Figs. 1 and 2a, respectively.

5.1 CO_2 injection

CO_2 is injected during seven years in the Utsira formation at a constant flow rate of one million tons per year. The injection point is located at the bottom of the formation: $x = 0.6$ km, $z = 1.082$ km. The simulation uses a mesh with equally-spaced blocks in each direction: $n_x = 300$ in the x-direction, $n_y = 5$ in the y-direction and $n_z = 400$ in the

z-direction. Actually the model is 2.5D since the properties are uniform along the y-direction, which has an extension of 10 km. It was checked that using a finer mesh in the y-direction did not dramatically change the output of the CO_2 injection simulation. The source is located at the third grid point along this direction. To satisfy the CFL stability condition due to IMPES formulation [20], the time step is 0.125 d. With this choice of the mesh and time step, we check that the results of the BOAST simulator satisfy the mass conservation condition. Recall that the petrophysical properties of the formation are time dependent due to the CO_2 injection and consequent increase in pore pressure (c.f. Eqs. 16, 17, and 18) but they change at a much slower rate than pressure and saturations. As a consequence, we have two time scales,

Fig. 9 CO_2 saturation distribution after 7 years of CO_2 injection without updating the petrophysical properties
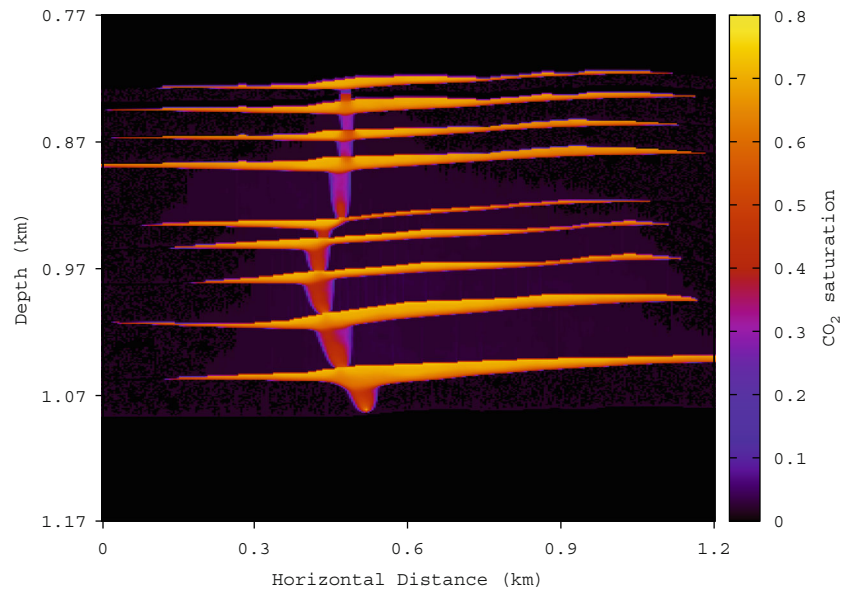

and we use a much larger time step to update petrophysical properties than to run the flow simulator. In this work, the petrophysical properties are updated every year.

Figure 3 a, b and c shows 2D vertical slices (corresponding to $n_y = 3$) of the CO_2 saturation fields after one, three and seven years of CO_2 injection, respectively. In all the cases, CO_2 accumulations below the mudstone layers can be observed. As injection proceeds, part of the injected fluid migrates upwards due to the openings in the mudstone layers that generate chimneys, and the vertical fluid flow is ruled by the vertical permeability. As CO_2 saturation increases, vertical permeability updated with Eq. 18 also increases, in particular in the mudstone layers. This allows an increase in the CO_2 upward motion across the

layers with the resulting low CO_2 saturations levels observed between layers. As a consequence, CO_2 chimneys become less defined as injection time increases, as it can be seen in Figs. 3 a, b and c. A 2D slice (at $n_y = 3$) of the saturation dependent vertical permeability distribution after seven years of CO_2 injection is shown in Fig. 2b. Porosity and horizontal permeability depending only on pressure suffer little changes and are not shown for brevity. Figure 4 displays the difference between CO_2 and brine pressure (capillary pressure) after seven years of injection. As CO_2 saturation increases, flow is more affected by capillary forces.

Summarizing, the presence of the CO_2 plume is due to the combination of three causes: the presence of physical

Fig. 10 CO_2 saturation distribution after 7 years of CO_2 injection for the case of high porosity and permeability fractal variations
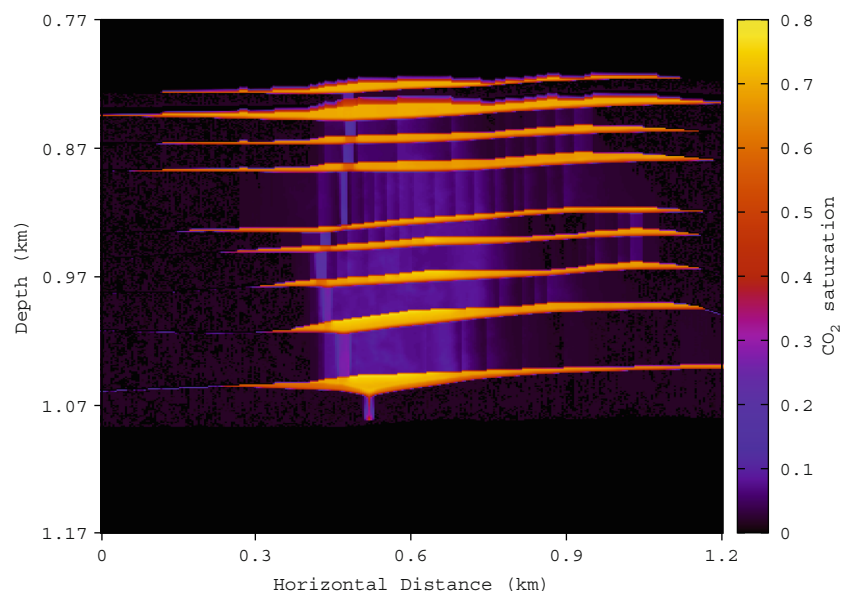
openings within the mudstone layers, the updating of the vertical permeability (see Eq. 18) and the increase of the CO_2 relative permeability as CO_2 content increases (see Eq. 21).

5.2 Seismic monitoring

In this section, we analyze the capability of seismic monitoring to identify zones of CO_2 accumulation and migration. With this purpose, we use 2D slices of CO_2 saturation and fluid pressure obtained from the flow simulator to construct a 2D model of the Utsira formation. The iterative procedure given in Eqs. 31–32 is used to compute the time Fourier transforms of the displacement vector for 200 equally spaced temporal frequencies in the interval (0, 200Hz). The seismic source is a spatially localized plane wave of main frequency 60 Hz located at $z = 772$ m. A line of receivers is located at the same depth to record the Fourier transforms of the vertical displacements. Then, a discrete inverse Fourier transform is applied to obtain the data used for the synthetic seismograms. The plane-wave simulation (a flat row of point sources at each grid point at the surface) is a good approximation to the stack. We could compute the stack explicitly by computing n common shots and then performing the (more expensive) standard processing sequence but this is not the main goal of this work. The plane-wave method is a good approximation [29].

Now, we proceed to compare the initial and perturbed velocity model in order to show how the presence of the accumulation of CO_2 below the mudstone layers and the CO_2 plume changes the seismic response of the formation, and, in particular, to accurate reproduce the pushdown effect observed in real seismograms.

Initially, we show the pre-injection results at full brine saturation. Figures 5a and 6a display the spatial distribution of the P-wave phase velocity v_P and S-wave phase velocity v_S before CO_2 injection. On the other hand, Figs. 5b and 6b display P and S-wave phase velocities v_P and v_S after seven years of CO_2 injection, predicted by White's model. It can be observed the reduction in the P-wave velocities in zones of CO_2 accumulation. Besides Fig. 7 shows the quality factor Q_p for P-waves. Notice that lower values of Q_p (higher attenuation) can be observed in regions of CO_2 accumulation.

Figure 8a shows the synthetic seismogram before the injection, where the mudstone layers in Figs. 5a and 6a are clearly identified.

Figure 8b, c and d displays non-migrated seismic sections after one, three and seven years of CO_2 injection associated with the CO_2 saturations shown in Figs. 3a, b and c, respectively. The figure show diffractions associated with
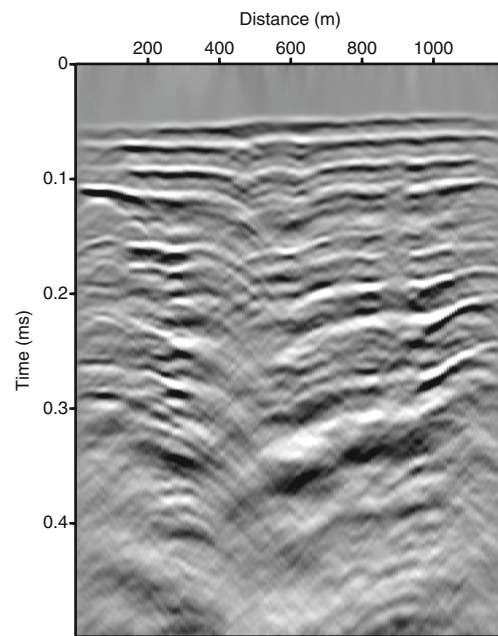

Fig. 11 Synthetic seismogram after seven years of CO_2 injection without updating the petrophysical properties

the presence of the low velocity CO_2 lenses. A standard f-k filter is used to eliminate some spurious reflections from the artificial boundaries of the computational mesh, since the absorbing boundary conditions used are only first order and can not eliminate all undesired boundary reflections.

The reflections seen in those seismograms show the progressive increase in CO_2 accumulations below the mudstone layers and in the chimneys as the injection proceeds. The progressive replace of brine by CO_2 causes a delay in the arrival times of the reflections and strong attenuation in the chimney region. In particular, the pushdown effect observed in the real seismograms [15] due to CO_2 accumulations is clearly observed (Fig. 8d).

6 Sensitivity analysis

In this section, some of the parameters used in the fluid flow and wave propagation simulators are perturbed in order to analyze their effect on the resulting CO_2 saturation maps and synthetic seismic sections.

6.1 Changes in the fluid flow parameters

In order to analize the effect of updating the petrophysical properties in the resulting saturation flow fields, we simulate 7 years of CO_2 injection without updating those
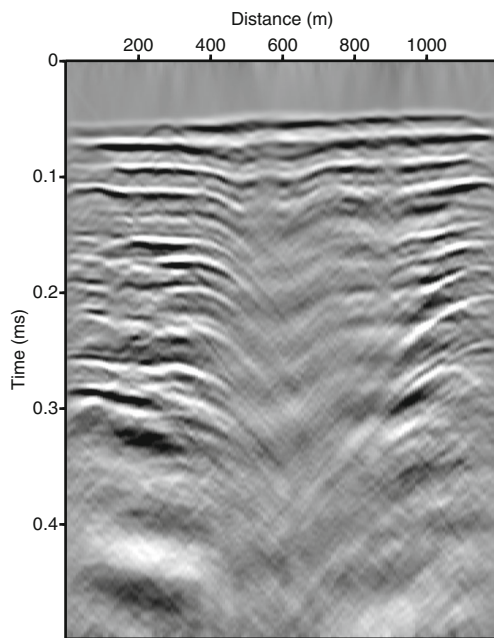
Fig. 12 Synthetic seismogram after seven years of CO_2 injection for the case of high porosity and permeability fractal variations

properties. The corresponding CO_2 saturation distribution can be observed in Fig. 9. As vertical permeability remains unchanged, the CO_2 saturation field shows very well defined chimneys associated with the openings of the mudstone layers; this saturation map is quite different to the one displayed in Fig. 3c.

Besides, a model with a high fractal porosity and permeability variations (and updating the petrophysical properties) is also considered. The CO_2 saturation distribution after seven years of injection is shown in Fig. 10. The comparison with Fig. 3c shows that high porosity and permeability variations do not change significantly the CO_2 distribution within the Utsira formation.

6.2 Changes in the seismic parameters

First, we analyze the case when the petrophysical properties are not updated. The corresponding synthetic seismogram after seven years of CO_2 injection is shown in Fig. 11. It is observed that the pushdown effect is not as well defined as in Fig. 8d. This can be explained by observing the saturation maps in Figs. 3c and 9. Figure 3c exhibits wider zones of low CO_2 saturation in the chimney region and between the mudstone layers causing a decrease in the P-wave velocities, which in turn emphasizes the pushdown effect.

Furhermore, we run wave propagation simulations for the case of high porosity and permeability fractal variations.

Figure 12 displays the corresponding seismogram after seven years of CO_2 injection. The pushdown effect can still be observed, but not as well defined as in Fig. 8d. This may be explained by the higher variations in petrophysical properties with the corresponding increase of scattering of the reflected waves.

7 Conclusions

We have performed numerical simulations of CO_2-brine flow and seismic wave propagation to model and monitor CO_2 storage in a saline aquifer. The flow simulator considers the CO_2 solubility in brine through a simplified thermodynamic model, with CO_2 properties determined by the Peng-Robinson equations. We have built a petrophysical model of a shaly sandstone based on fractal porosity and considering the variation of its properties with pore pressure and fluid saturation. The wave propagation simulator takes into account wave velocity dispersion and attenuation effects due to the presence of mesoscopic scale heterogeneities caused by patches of carbon dioxide. The proposed methodology has been applied to the Utsira formation, which contains several thin low-permeability mudstone layers. These layers are not completely sealed and also have openings, allowing the upward migration of CO_2.

The fluid-flow simulator yields CO_2 accumulations below the mudstone layers. Taking into account the time-lapse variations of the petrophysical properties (with vertical permeability being the more affected property by this updating), the corresponding synthetic seismograms resemble the real seismic data. In particular, regions of low saturations between layers and less defined chimneys are obtained. The reflections seen in the seismograms show the progressive increase in CO_2 accumulations below the mudstone layers, in particular, the pushdown effect is clearly observed.

When high variations of petrophysical properties are assumed, the seismic response is masked by the increase of scattering of the reflected waves and the pushdown effect is less noticiable. The pushdown effect is not evident when the petrophysical properties are not updated.

Summarizing, this methodology constitutes an important tool to monitor the migration and dispersal of the CO_2 plume, to analyze storage integrity and to make long term predictions.

Appendix A - IMPES solution for black-oil formulation

The IMPES technique combines the flow Eqs. 6–7 to obtain a single pressure equation. In this way, Eq. 6 multiplied by B_g and Eq. 7 multiplied by $(B_b - R_s B_g)$ are added. The right-hand side of the combined equation results,

$$
B_g \frac{\partial \left[\phi \left(\frac{S_g}{B_g} + \frac{R_s S_b}{B_b} \right) \right]}{\partial t} + (B_b - R_s B_g) \frac{\partial \left[\phi \frac{S_b}{B_b} \right]}{\partial t}. \tag{27}
$$

Using the chain rule to expand the time derivatives, and after some algebraic manipulations, the expression in Eq. 27 becomes:

$$
\phi \left[\frac{1}{\phi} \frac{d\phi}{dp_b} + S_g \left(-\frac{1}{B_g} \frac{dB_g}{dp_b} \right) + S_b \left(-\frac{1}{B_b} \frac{dB_b}{dp_b} + \frac{B_g}{B_b} \frac{dR_s}{dp_b} \right) \right] \frac{\partial p_b}{\partial t}, \tag{28}
$$

where all time derivatives of saturation have disappeared. Defining the compressibilities as

Formation compressibility: $c_f = \frac{1}{\phi} \frac{d\phi}{dp_b}$,

Gas compressibility: $c_g = -\frac{1}{B_g} \frac{dB_g}{dp_b}$,

Brine compressibility: $c_b = -\frac{1}{B_b} \frac{dB_b}{dp_b} + \frac{B_g}{B_b} \frac{dR_s}{dp_b}$,

Total compressibility: $c_t = c_f + S_g c_g + S_b c_b$,

the following simply expression is obtained for the right-hand side of the combined equation,

$$
\phi c_t \frac{\partial p_b}{\partial t}. \tag{29}
$$

Finally, replacing p_g by $p_b + P_C(S_b)$ in the left side of the combined equation, the pressure Eq. 9 is obtained.

Appendix B - The iterative domain decomposition algorithm

B1. Weak formulation

We proceed to formulate the variational form for viscoelastic waves:

Find an approximate solution $\widehat{u} \in [H^1(\Omega)]^2$ such that

$$
-(\rho\omega^2\widehat{u}, \varphi) + \sum_{pq}(\sigma_{pq}(\widehat{u}), \varepsilon_{pq}(\varphi)) + i\omega \langle \mathcal{D}\widehat{u}, \varphi \rangle_\Gamma = (\widehat{f}, \varphi), \quad \varphi \in [H^1(\Omega)]^2.
$$

where φ are the test functions.

Here $(f, g) = \int_\Omega f\overline{g}\,d\Omega$ and $\langle f, \overline{g} \rangle = \int_\Gamma f\overline{g}\,d\Gamma$ denote the complex $[L^2(\Omega)]^N$ and $[L^2(\Gamma)]^N$ inner products. Also, $H^1(\Omega)$ denotes the usual Sobolev space of functions in $L^2(\Omega)$ with first derivatives in $L^2(\Omega)$.

B2. Finite element method

To define a global finite element method, we use the nonconforming finite element space based on rectangular elements first presented in [30] described below. For $h > 0$, let $\mathcal{T}_h$ be a quasiregular partition of $\overline{\Omega}$ such that $\overline{\Omega} = \cup_{j=1}^J \overline{\Omega}_j$ with Ω_j being rectangles of diameter bounded by h. Set $\Gamma_j = \partial\Omega \cap \partial\Omega_j$ and $\Gamma_{jk} = \Gamma_{kj} = \partial\Omega_j \cap \partial\Omega_k$, we denote by ξ_j and ξ_{jk} the centroids of Γ_j and Γ_{jk}, respectively.

We consider a nonconforming finite element space constructed using the following reference rectangular element:

$$
\widehat{R} = [-1, 1]^2 \qquad S_2(\widehat{R}) = \mathrm{Span}\left\{ \frac{1}{4} \pm \frac{1}{2}x - \frac{3}{8}\left((x^2 - \frac{5}{3}x^4) - (y^2 - \frac{5}{3}y^4) \right), \right.
$$
$$
\left. \frac{1}{4} \pm \frac{1}{2}y + \frac{3}{8}\left((x^2 - \frac{5}{3}x^4) - (y^2 - \frac{5}{3}y^4) \right) \right\}.
$$

The four degrees of freedom associated with $S_2(\widehat{R})$ are the values at the mid points of the faces of $\widehat{R}$, i.e., the values at the nodal points $a_1 = (-1, 0), a_2 = (0, -1), a_3 = (1, 0)$ and $a_4 = (0, 1)$. For example the basis function $\psi_1(x, y) = \frac{1}{4} - \frac{1}{2}x - \frac{3}{8}\left((x^2 - \frac{5}{3}x^4) - (y^2 - \frac{5}{3}y^4) \right)$ is such that $\psi_1(a_1) = 1$ and $\psi_1(a_j) = 0$, $j = 2, 3, 4$.

Set $NC_j^h = S_2(\Omega_j)$ and define a nonconforming finite element space in the following manner

$$
NC^h = \left\{ v \mid v_j := v\mid_{\Omega_j} \in NC_j^h, j = 1, \dots, J; \right.
$$

$$
\left. v_j(\xi_{jk}) = v_k(\xi_{jk}), \ \forall\{j, k\} \right\}.
$$

The global nonconforming Galerkin procedure is defined as follows: find $\widehat{u}^h \in [NC^h]^2$ such that

$$
-(\rho\omega^2\widehat{u}^h, \varphi) + \sum_{pq}(\tau_{pq}(\widehat{u}^h), \varepsilon_{pq}(\varphi))
$$
$$
+i\omega \left\langle\!\!\left\langle \mathcal{D}\widehat{u}^h, \varphi \right\rangle\!\!\right\rangle_\Gamma = (\widehat{f}, \varphi), \varphi \in [NC^h]^2, \tag{30}
$$

where $\langle\!\langle \cdot, \cdot \rangle\!\rangle$ denotes the approximation of $\langle \cdot, \cdot \rangle$ on the boundary faces by the midpoint quadrature rule.

A useful property of applying nonconforming elements for wave propagation phenomena is that it almost halves the number of points per wavelength necessary to reach a given accuracy as compared with the standard bilinear elements [31]. Note that the global algebraic problem asociated with Eq. 30 has more degrees of freedom than if standard bilinear elements were used, but we never solve the global problem for each frequency. Instead, taking advantage that we have a dissipative media and absorbing boundary conditions are used, we solve local problems at the computational cell level using the parallelizable domain decomposition iterative hybridized procedure defined in [21] and briefly described below. Note that at computational cell level the number of degrees of freedom is the same for both conforming and nonconforming elements, but while for the nonconforming case a rate of convergence of the iteration in terms of the subdomain size h can be demonstrated [21], this result can not be proved for bilinear elements. Besides, the iterative domain decomposition based on noncorforming elements is naturaly parallelizable, and the amount of information needed to be exchanged among processors is about half if bilinear elements were used, as it is explained in [31]. This approach becomes a necessity when dealing with very large 2D (or 3D) problems.

To define the iterative procedure, we introduce a set $\widetilde{\Lambda}^h$ of Lagrange multipliers λ_{jk}^h associated with the stress values $-\tau(\widehat{u}_j)\nu_{jk}(\xi_{jk})$:

$$\widetilde{\Lambda}^h = \{\lambda^h : \lambda^h|_{\Gamma_{jk}} = \lambda_{jk}^h \in [P_0(\Gamma_{jk})]^2 = [\Lambda_{jk}^h]^2\}.$$

Here $P_0(\Gamma_{jk})$ are constant functions on Γ_{jk}. Note that Λ_{jk}^h and Λ_{kj}^h are considered to be distinct.

Then, given an initial guess $\left(\widehat{u}_j^{h,0}, \lambda_{jk}^{h,0}, \lambda_{kj}^{h,0}\right) \in [NC_j^h]^2 \times [\Lambda_{jk}^h]^2 \times [\Lambda_{kj}^h]^2$, compute $\left(\widehat{u}_j^{h,n}, \lambda_{jk}^{h,n}\right) \in [NC_j^h]^2 \times [\Lambda_{jk}^h]^2$ as the solution of the equations

$$-(\rho\omega^2\widehat{u}_j^{h,n}, \varphi)_j + \sum_{pq}(\tau_{pq}(\widehat{u}^{h,n}), \varepsilon_{pq}(\varphi))_j$$
$$+i\omega\left\langle\!\!\left\langle \mathcal{D}\widehat{u}_j^{h,n}, \varphi \right\rangle\!\!\right\rangle_{\Gamma_j} + \sum_k \left\langle\!\!\left\langle \lambda_{jk}^{h,n}, \varphi \right\rangle\!\!\right\rangle_{\Gamma_{jk}} = (\widehat{f}, \varphi)_j,$$
$$\varphi \in [NC_j^h]^2, \qquad (31)$$

$$\lambda_{jk}^{h,n} = -\lambda_{kj}^{h,n-1}$$
$$+i\beta_{jk}[\widehat{u}_j^{h,n}(\xi_{jk}) - \widehat{u}_k^{h,n-1}(\xi_{jk})], \quad \text{on } \Gamma_{jk}. \qquad (32)$$

It can be shown that

$$[\widehat{u}^{h,n} - \widehat{u}^h]^2 \to 0 \text{ in } [L^2(\Omega)]^2 \quad \text{when} \quad n \to \infty,$$

so that in the limit the global nonconforming Galerkin approximation is obtained [21].

Appendix C - Estimation of brine density and CO_2 mole and mass fractions in the brine phase

The brine mass density at reservoir conditions is estimated using the approach of García [8], as follows,

$$\rho_b = \frac{1 + (M_g/M_b)(\chi_g/(1-\chi_g))}{(V_m/M_b)(\chi_g/(1-\chi_g)) + 1/\rho_b^{SC}}, \qquad (33)$$

where M_g, M_b are the CO_2 and brine molecular weights, respectively; χ_g is the CO_2 mole fraction in the brine phase; ρ_b^{SC} is the brine mass density at standard conditions and V_m is a partial molar volume, computed as a function of temperature T (°C) as in formula (21) of [8]:

$$V_m = 37.51 - 9.585 x 10^{-2} T + 8.74 x 10^{-4} T^2 - 5.044 x 10^{-7} T^3. \qquad (34)$$

To determine χ_g, we apply the following relationship

$$\chi_g = \frac{m_g}{m_g + 55.508 + \nu m_s}, \qquad (35)$$

where m_g is the molality of CO_2 in saline water, m_s is the salt molality and ν is the stoichiometric number of ions in the dissolved salt. In order to compute m_g we use

$$m_g = \frac{m_g^o}{\gamma_g^*}, \qquad (36)$$

where m_g^o is the molality of CO_2 in pure water and γ_g^* the activity coefficient.

To obtain m_g^o for each pressure and temperature, we solve iteratively the thermodynamic nonlinear equations (B1)-(B5) in [8]. These equations involve H_2O and CO_2 molar volumes, fugacities and activity coefficients. The CO_2 molar volume is computed using the Peng-Robinson model [25]. Also, γ_g^* is obtained using the Rumpf model, as stated in equation (A6) in Spycher & Pruess [27].

Once χ_g is computed, the CO_2 mass fraction in the aqueous phase ω_g is obtained from the relation:

$$\omega_g = \chi_g \frac{M_g}{M_{aq}}. \qquad (37)$$

Here M_{aq} is the aqueous molecular weight, given by

$$M_{aq} = \chi_g M_g + \chi_{H_2O} M_{H_2O} + \chi_{salt} M_{salt}. \qquad (38)$$

References

1. Arts, R., Chadwick, A., Eiken, O., Thibeau, S., Nooner, S.: Ten years of experience of monitoring CO_2 injection in the Utsira sand at Sleipner, offshore Norway. First Break **26**, 65–72 (2008)

2. Chadwick, A., Arts, R., Eiken, O.: 4D seismic quantification of a growing CO_2 plume at Sleipner, North Sea. In: Dore, A.G., Vincent, B. (eds.) Petroleum Geology: North West Europe and Global Perspectives - Proc. 6th Petroleum Geology Conference, pp. 1385–1399 (2005)

3. Carcione, J.M., Picotti, S.: P-wave seismic attenuation by slow-wave diffusion: Effects of inhomogeneous rock properties. Geophysics **71**(3), O1–O8 (2006)

4. Santos, J.E., Rubino, J.G., Ravazzoli, C.L.: Modeling mesoscopic attenuation in a highly heterogeneous Biot's medium employing an equivalent viscoelastic model. Proceedings of the 78th Annual International Meeting SEG, 9-14 November, Las Vegas, USA, 2212–2215 (2008)

5. Picotti, S., Carcione, J.M., Gei, D., Rossi, G., Santos, J.E.: Seismic modeling to monitor CO_2 geological storage: The Atzbach-Schwanenstadt gas field. J. Geophys. Res. **117**, B06103 1–18 (2012)

6. Carcione, J.M., Helbig, K., Helle, H.B.: Effects of pressure and saturating fluid on wave velocity and attenuation of anisotropic rocks. Int. J. Rock Mech. Min. Sci. **40**, 389–403 (2003)

7. Aziz, K., Settari, A.: Petroleum Reservoir Simulation. Elsevier Applied Science Publishers, Great Britain (1985)

8. Hassanzadeh, H., Pooladi-Darvish, M., Elsharkawy, A., Keith, D., Leonenko, Y.: Predicting PVT data for CO_2-brine mixtures for black-oil simulation of CO_2 geological storage. Int. J. Greenhouse Gas Control **2**, 65–77 (2008)

9. Muller, T., Gurevich, B., Lebedev, M.: Seismic wave attenuation and dispersion resulting from wave-induced flow in porous rocks – a review. Geophysics **75**, A147–A164 (2010)

10. Pride, S., Berryman, J., Harris, J.: Seismic attenuation due to wave-induced flow. J. Geophys. Res. **109**, B01201 (2004). doi:10.1029/2003JB002639

11. Picotti, S., Carcione, J., Rubino, G., Santos, J., Cavallini, F.: A viscoelastic representation of wave attenuation in porous media. Comput. Geosci. **36**, 44–53 (2010)

12. Carcione, J.M.: Wave Fields in Real Media. Theory and Numerical Simulation of Wave Propagation in Anisotropic, Anelastic, Porous and Electromagnetic Media, Elsevier, Third edition, revised and extended (2014)

13. White, J.E., Mikhaylova, N.G., Lyakhovitskiy, F.M.: Low-frequency seismic waves in fluid-saturated layered rocks. Izvestija Academy of Sciences USSR. Phys. Solid Earth **10**, 654–659 (1975)

14. Dai, N., Vafidis, A., Kanasewich, E.R.: Wave Propagation in heterogeneous, porous media: A velocity stress, finite difference method. Geophysics **60**(2), 327–340 (1995)

15. Chadwick, R.A., Noy, D., Arts, R., Eiken, O.: Latest time-lapse seismic data from Sleipner yield new insights into CO_2 plume development. Energy Procedia, 2103–2110 (2009)

16. Chadwick, R.A., Williams, G., Delepine, N., Clochard, V., Labat, K., Sturton, S., Buddensiek, M., Dillen, M., Nickel, M., Lima, A., Arts, R., Neele, F., Rossi, G.: Quantitative analysis of time-lapse seismic monitoring data at the Sleipner CO_2 storage operation. Lead. Edge **29**, 170–177 (2010)

17. Jones, K.: On the differential form of Darcy's law. J. Geophys. Res. **67**(2), 731–732 (1962)

18. Bear, J.: Dynamics of fluids in porous media. American Elsevier Publishing Company, New York (1972)

19. Fanchi, J.: Principles of Applied Reservoir Simulation. Gulf Professional Publishing Company, Houston (1997)

20. Savioli, G., Bidner, M.S.: Simulation of the oil and gas flow toward a well - a stability analysis. J. Pet. Sci. Eng. **48**, 53–69 (2005)

21. Ha, T., Santos, J.E., Sheen, D.: Nonconforming finite element methods for the simulation of waves in viscoelastic solids. Comput. Meth. Appl. Mech. Engrg. **191**, 5647–5670 (2002)

22. Carcione, J., Gurevich, B., Cavallini, B.F.: A generalized Biot-Gassmann model for the acoustic properties of shaley sandstones. Geophys. Prosp. **48**, 539–557 (2000)

23. Hashin, Z., Shtrikman, S.: A variational approach to the elastic behavior of multiphase minerals. J. Mech. Phys. Solids **11**(2), 127–140 (1963)

24. Krief, M., Garat, J., Stellingwerff, J., Ventre, J.: A petrophysical interpretation using the velocities of P and S waves (full waveform sonic). Log Anal. **31**, 355–369 (1990)

25. Peng, D.Y., Robinson, K.I.: A new two-constant equation of state. Ind. Eng. Chem. Fundam. **15**(1), 59–64 (1976)

26. Santos, J.E., Savioli, G., Macias, L., Carcione, J., Gei, D.: Influence of capillary pressure on CO2 storage and monitoring. Proceedings of the 84th Annual International Meeting SEG, 26-31 October, Denver, USA, 2212–2215 (2014)

27. Spycher, N., Pruess, K.: CO_2-H_2O mixtures in the geological sequestration of CO_2. II. Partitioning in chloride brines at 12-100 C and up to 600 bar. Geochim. Cosmochim, Acta **69**(13), 3309–3320 (2005)

28. Frankel, A., Clayton, R.W.: Finite difference simulation of seismic wave scattering: implications for the propagation of short period seismic waves in the crust and models of crustal heterogeneity. J. Geophys. Res. **91**, 6465–6489 (1986)

29. Carcione, J.M., Böehm, G., Marchetti, A.: Simulation of a CMP seismic section. J. Seism. Explor. **3**, 381–396 (1994)

30. Douglas, J.Jr., Santos, J.E., Sheen, D., Ye, X.: Nonconforming Galerkin methods based on quadrilateral elements for second order elliptic problems. RAIRO Math. Model Numer. Anal. (M2AN) **33**, 747–770 (1999)

31. Zyserman, F.I., Gauzellino, P.M., Santos, J.E.: Dispersion analysis of a non-conforming finite element method for the Helmholtz and elastodynamic equations. Int. J. Numer. Meth. Engng. **58**, 1381–1395 (2003)